# 60-GHz Millimeter-Wave Channel Measurements and Modeling for Indoor Office Environments

Xianyue Wu, *Member, IEEE*, Cheng-Xiang Wang, *Fellow, IEEE*, Jian Sun, *Member, IEEE*, Jie Huang,
Rui Feng, Yang Yang, *Senior Member, IEEE*, and Xiaohu Ge, *Senior Member, IEEE*

*Abstract*—The millimeter-wave (mmWave) band will be used for the fifth-generation communication systems. In this paper, 60-GHz mmWave channel measurements and modeling are carried out for indoor office environments. The rotated directional antenna-based method and uniform virtual array-based method are adopted and compared to investigate the 60-GHz channel in a 3-D space, simultaneously covering azimuth and coelevation domains. The multipath component parameters including power, delay, azimuth, and elevation angles are estimated with the space-alternating generalized expectation–maximization estimation algorithm, and then processed with the K-means clustering algorithm. An extended Saleh–Valenzuela model with both delay and angular cluster features is used to characterize the measured channel, and the intercluster and intracluster parameters are extracted. We find that the azimuth departure angles are diverse and highly related to the antenna position and measurement environment, while the elevation departure angles are more related to the antenna height difference and confined in a relatively small direction range. The azimuth angle spread is much larger than the elevation angle spread either in global level or in cluster level. The results agree with the studies in the literature and channel models in IEEE standards.

*Index Terms*—60-GHz millimeter-wave (mmWave) channels, channel measurements, parameter estimation, Saleh–Valenzuela (S-V) channel model, space-alternating generalized expectation–maximization (SAGE) algorithm.

X. Wu was with Institute of Sensors, Signals and Systems, School of Engineering and Physical Sciences, Heriot-Watt University, Edinburgh EH14 4AS, U.K. He is now with Huawei Technologies Co., Ltd., Shanghai Research Institute, Shanghai 200120, China (e-mail: wuxianyue@huawei.com).

C.-X. Wang is with Shandong Provincial Key Lab of Wireless Communication Technologies, School of Information Science and Engineering, Shandong University, Jinan 250100, China, and also with the Institute of Sensors, Signals and Systems, School of Engineering and Physical Sciences, Heriot-Watt University, Edinburgh EH14 4AS, U.K. (e-mail: cheng-xiang.wang@hw.ac.uk).

J. Sun is with the Shandong Provincial Key Lab of Wireless Communication Technologies, School of Information Science and Engineering, Shandong University, Shadong 250100, China, and also with State Key Laboratory of Millimeter Waves, Southeast University, Nanjing 210096, China (e-mail: sunjian@sdu.edu.cn).

J. Huang and R. Feng are with Shandong Provincial Key Lab of Wireless Communication Technologies, School of Information Science and Engineering, Shandong University, Shadong 250100, China (e-mail: hj1204@sina.cn; fengxiurui604@163.com).

Y. Yang is with the Key Laboratory of Wireless Sensor Network and Communication, Shanghai Institute of Microsystem and Information Technology, Chinese Academy of Sciences, Shanghai 200050, China, and also with the Shanghai Research Center for Wireless Communications, Shanghai 201210, China (e-mail: yang.yang@wico.sh).

X. Ge is with the School of Electronic Information and Communications, Huazhong University of Science and Technology, Wuhan 430074, China (e-mail: xhge@mail.hust.edu.cn).

Color versions of one or more of the figures in this paper are available online at http://ieeexplore.ieee.org.

Digital Object Identifier 10.1109/TAP.2017.2669721

## I. INTRODUCTION

WIRELESS communication networks are facing new challenges as Internet usages are proliferating. Future networks have to support high capacity, high mobility [1], and massive connectivity with increasingly diverse set of services, applications, and users [2], such as machine-to-machine and Internet of things, to enable communications anywhere, anytime, and by anything. Also, the flexible and efficient use of all spectrums and resources are required to accommodate widely different network deployment scenarios. These requirements have been envisioned for the research and development of the fifth-generation (5G) wireless communication systems. To address these challenges, there has been growing interest in moving up frequency into millimeter-wave (mmWave) bands where enormous bandwidths are available. MmWave technologies can achieve much higher data rate by using simple air interfaces due to the large bandwidth. In addition, by virtue of the vast available and unlicensed bandwidth, mmWave systems can satisfy higher system capacity requirement [3]. The mmWave band has drawn increasing attention despite earlier hiccups associated with the cost of producing commercial products [4]. With advances in mmWave chipset manufacturing led by, among others, Intel and IBM, this band has been opened up by various regulatory authorities in the process of developing the first 60-GHz mmWave standards and specifications such as IEEE 802.15.3c [5] for wireless personal area networks and IEEE 802.11ad [6] for multigigabit wireless local area networks.

The propagation characteristics at mmWave bands are quite different from those at frequency bands below 6 GHz. Because of small wavelengths at mmWave bands, diffraction becomes the weakest and least reliable propagation mechanism for mmWave communication systems. Many small objects in the environment can be considered as scatterers, thus exhibiting a highly reflective and scattering nature to create alternative viable links, except for the direct link [7]. Also, atmospheric attenuation caused by air and water molecules creates additional path loss (PL) at mmWave frequencies, especially at

60 GHz. In addition, with identical antenna gains and transmit powers, the power received at mmWave bands is smaller than that at lower frequencies due to the smaller antenna aperture. Due to these propagation characteristics, highly directional antennas, large antenna array, and adaptive beamforming techniques may be used to establish reliable communication links in mmWave wireless communication systems [8].

Recently, there have been extensive research on mmWave outdoor cellular communications. In [9]–[11], the measurements were conducted at 28, 38, and 73 GHz in urban outdoor environments. These studies mainly focused on large-scale properties of wireless channels. Results show that by using directional or adaptive beamforming antennas, mmWave signals are potentially viable at distances of 100–200 m, even in nonline-of-sight (NLOS) scenarios. Besides, mmWave systems can provide at least an order of magnitude improvement in capacity over long-term evolution systems, at least for outdoor coverage.

Current cellular communication systems normally use an outdoor base station (BS) in the middle of a cell to communicate with mobile users, no matter whether they stay indoors or outdoors. For indoor users communicating with an outdoor BS, the signals have to go through building walls, which cause very high penetration loss that significantly degrades the data rate, spectral efficiency, and energy efficiency of wireless transmissions. At mmWave frequencies, this situation will be even worse. Therefore, outdoor and indoor scenarios will be probably separated in 5G cellular architecture [12].

Extensive channel measurement campaigns at mmWave frequencies have been conducted in indoor environments, especially at 60 GHz [13]–[16]. Large-scale properties like PL and delay dispersion at mmWave frequencies in indoor channels have been studied thoroughly [15], [17], [18]. Studies show that the PL exponent $n$ varies from 0.40 to 2.10 and from 1.97 to 5.40 for line-of-sight (LOS) and NLOS scenarios, respectively, in various 60-GHz indoor environments. Specifically, in a typical office environment, $n$ takes values in the ranges from 1.16 to 2.17 and from 2.83 to 4.00 for LOS and NLOS scenarios, respectively [19]. Delay dispersion is affected by the dimensions of the room, the wall reflection coefficient, and antenna polarization and beamwidth [13], [20]. With respect to channel modeling for 5G mmWave indoor communication systems, the characteristics of both azimuth and elevation angles in 3-D space, large antenna array, super-high resolution in delay domain, and small-scale fading characteristics should be considered.

Angular characteristics of multipath propagation are critical for mmWave communication systems that exploit highly directional steering antennas and adaptive array. In general, there are two kinds of measurement methods for indoor mmWave channel angular characterization. One is the rotated directional antenna (RDA)-based method and the other is the uniform virtual array (UVA)-based method. Both methods are only applied to quasi-static environment due to the long time required for the antenna to scan directions or shift positions in the 3-D space. In the RDA-based method, a highly directional antenna is used with a vector network analyzer (VNA) or channel sounder. The antenna is placed

on the positioner and scanned in the azimuth and elevation angular domains with a small rotation angle step during the measurements. Because of the narrow beamwdith of the antenna, the antenna pointing angle is taken as the angle of arrival (AoA) or angle of departure (AoD) of multipath components (MPCs) [21]. In the UVA-based method, the RDA is replaced by an omnidirectional antenna which shifts position in the 3-D space with a step less than a half wavelength [22]. For the estimation of UVA measurement channel MPC parameters, high-resolution parameter estimation algorithms like subspace-based multiple signal classification and estimation of signal parameters via rotational invariance technique algorithms, and maximum-likelihood (ML)-based space-alternating generalized expectation-maximization (SAGE) and Richter's ML parameter estimation framework algorithms are usually utilized to process the measurement data.

Two IEEE standards, 802.15.3c and 802.11ad, have been proposed for 60-GHz indoor wireless communications. IEEE 802.15.3c is a single-input multiple-output channel model and only characterizes the AoA in azimuth domain, while IEEE 802.11ad is a multiple-input multiple-output (MIMO) channel model and characterizes the double-directional angle properties. A detailed comparison of the channel models in two standards can be found in [23]. The channel models for both standards are based on the angular cluster extended Saleh–Valenzuela (S-V) model [24]. In this model, MPCs are clustered in both time and angular domains. The intercluster and intracluster characteristics are modeled statistically in [25] and [26]. The detailed S-V-based channel model parameterization at 60 GHz in various indoor environments can be found in [27]–[30]. Because high-gain directional antennas are supposed to be used at mmWave frequencies, further investigation of directional characterization is also required. Although the IEEE 802.15.3c and IEEE 802.11ad models provide certain directional information, additional measurements for verification in a variety of environments would be desirable. Also, current studies on directional characteristics mainly focus on azimuth domain, but elevation domain characteristics are also important due to the use of massive MIMO and large antenna array at mmWave frequencies. The contributions of this paper are as follows.

1) We investigate the 60-GHz indoor wireless channel in the 3-D space, which simultaneously covers azimuth and its coelevation domains using both the RDA-based method and UVA-based method. Detailed measurement setup and full comparison of the two methods are given. Good agreement is shown between the RDA measurement results and UVA estimation results in both LOS and NLOS scenarios. The estimated MPCs using the SAGE algorithm are presented.

2) We provide a 60-GHz channel model and its parameterization for office environment based on the angular extended S-V model and temporal and spatial clustering properties.

3) We model the channel in both intercluster and intracluster levels, especially in angular domains.

The remainder of this paper is organized as follows. Section II describes the measurement environment, mea-
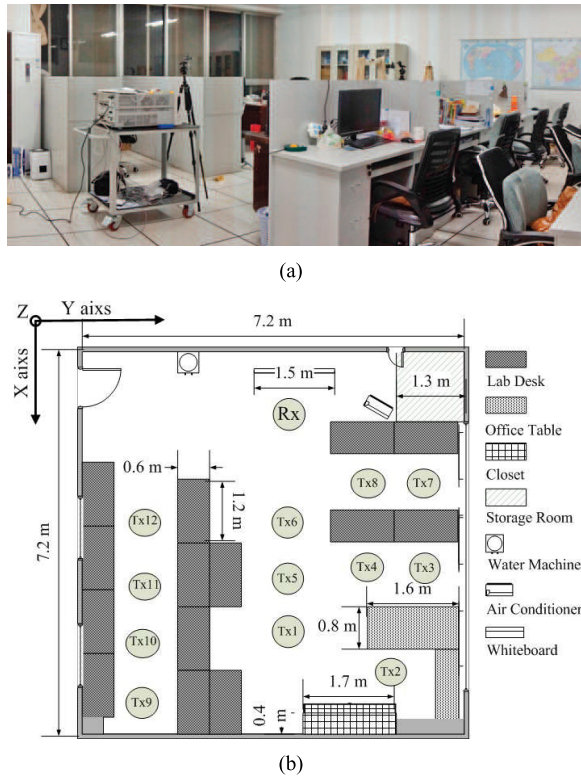
(a)



(b)

Fig. 1. (a) Photo of the office environment. (b) Layout of the office.

surement system setup, channel measurement methods, measurement methods' comparison, and SAGE algorithm. In Section III, the measured and estimated channel results for RDA- and UVA-based methods are presented and fully compared. The channel modeling and evaluation from the measurement results are described in Section IV. Finally, conclusions are drawn in Section V.

## II. 3-D INDOOR mmWAVE CHANNEL MEASUREMENTS
### A. Measurement Environment

The indoor measurements are conducted in an office environment as shown in Fig. 1(a), while the layout is shown in Fig. 1(b). The size of the room is about $7.2 \times 7.2 \times 3$ m$^3$. The office is furnished with multiple chairs, desks, and a table. The desks are about 0.75-m height at desktop level but with an additional vertical clapboard having about 0.45-m height. Thus, the total height is about 1.2 m. In addition, the desks and table are equipped with several computers and electronic devices. Other large objects include a closet, an air conditioner, a water machine, and a whiteboard. The walls, floor, and ceiling are made of concrete. Parts of the floor and ceiling are made of antistatic-electricity board. There are several windows on both sides of the wall. The locations of the 12 transmitter (Tx) and the receiver (Rx) in the UVA measurement are also labeled in Fig. 1(b). In the RDA measurement, the Rx position is the same with the UVA measurement while the Tx is located at Tx1 and Tx3.

### B. Measurement System Setup

The measurement system setup is shown in Fig. 2. A PC is used to control the antenna positioner through a universal
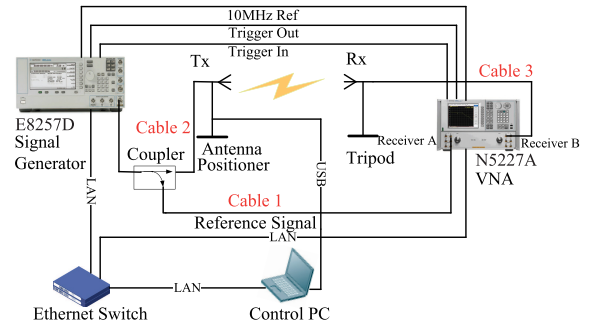


Fig. 2. Measurement system setup.

serial bus port. The PC also controls the Keysight E8257D analog signal generator and Keysight N5227A VNA through local area network ports. The analog signal generator and VNA are connected by 10-m-long trigger in/out and 10-MHz time base cables, thus achieving precise synchronization. With the signal generator, the measurable distance can be extended, and the measurement system does not need power amplifier, which may introduce noises into the measured channel data. The signal generator is used as the source whose output signal is split into two parts by a directional coupler. One part is fed to the Tx antenna as a channel sounding signal, and the other part is fed to the VNA as the reference signal. The VNA is used as the Rx which is connected with the Rx antenna by a coaxial cable. The customized high-precision antenna positioner has 5 degrees of freedom in the $X/Y/Z$/azimuth/elevation axes. Its scan ranges are $-180°$ to $180°$ in azimuth, $0°–180°$ in elevation, $\pm300$ mm in $X$-axis, $0–600$ mm in $Y$-axis, and $\pm250$ mm in $Z$-axis, as shown in Fig. 3. The antenna positioner is placed on the Tx side. With the antenna positioner, Tx antenna can scan in azimuth and elevation 3-D angular domains for the RDA measurements and scan in $X/Y/Z$ axes to form a 3-D virtual antenna array for the UVA measurements. At the Rx side, a tripod is used to support a fixed horn antenna. We define that the azimuth angle $\phi$ along $X$-axis is $0°$. It increases when rotating counterclockwise and decreases when rotating clockwise. Therefore, $\phi \in [-180°, 180°)$ is held. The elevation angle $\theta$ is defined to be $0°$ along $Z$-axis and it increases when rotating downward as shown in Fig. 3. So, $\theta \in [0°, 180°]$ is held.

### C. Channel Measurement Methods

*1) RDA Method:* The RDA-based measurement approach is to steer the highly directional antenna in azimuth and elevation domains in the measurement as shown in Fig. 4. This method has been used in [9], [10], and [21] for outdoor urban measurements, but the elevation pointing angles were very limited, for example, just pointed to $0°$ and $\pm10°$. The narrow beamwidth directional antenna divides the space into multiple sectors. In the measurement, both Tx and Rx antennas are 25-dBi standard gain horn antennas with E- and H-plane 3-dB beamwidth of $10°$ at 60 GHz. The Tx antenna is placed on the antenna positioner which is rotated from $-180°$ to $180°$ in azimuth angles and from $30°$ to $150°$ in elevation angles with the step of $5°$ in one snapshot of the channel measurements. Note that the intention of RDA method is to
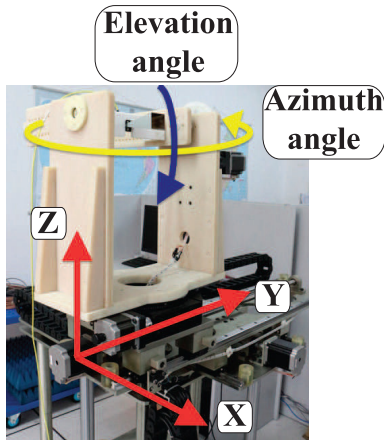
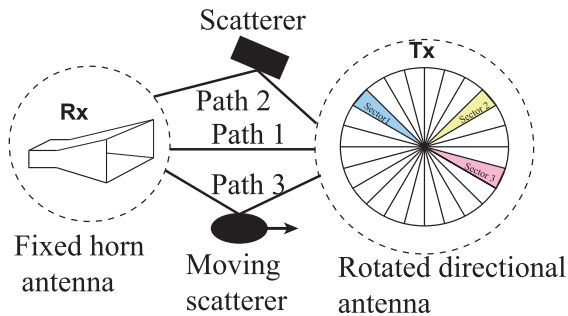Fig. 3. Antenna positioner with five axes ($X/Y/Z$/azimuth/elevation).

TABLE I
MEASUREMENT SETTINGS FOR THE RDA-BASED MEASUREMENT

| Center frequency 60 GHz | Bandwidth 2 GHz | Sampling points 401 | Output power +13 dBm |
|---|---|---|---|
| IF bandwidth 1 kHz | Tx locations and scan points in azimuth and elevation Tx1 and Tx3, $72 \times 25$ | Rx antenna gain and beamwidth 25 dBi, 10° | Rotation step angle 5° |



Fig. 4. RDA-based measurement method.
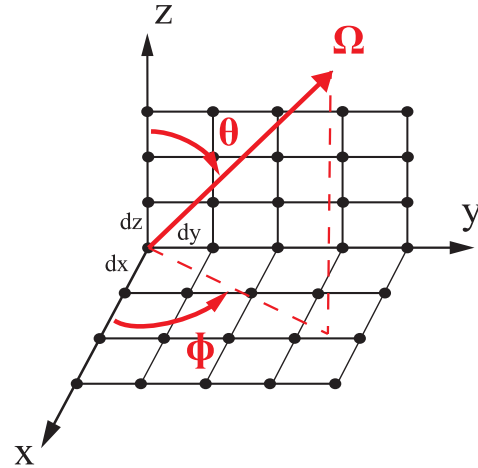


Fig. 5. UVA configuration and direction characterization.

achieve the omnidirectional coverage with high gain, and the antenna beamwidth and rotation step will have impact on the measurements. Actually, the same MPCs will appear across multiple adjacent angular bins, which will make troubles when discussing power angle spectrum (PAS). However, when we deal with the power delay profile (PDP), superposition of PDPs in every direction is equivalent to create a nearly flat antenna power response over all spatial directions. As shown in [31], the same 10° beamwidth horn antenna was rotated with step size of 10° and the virtual antenna array was formulated. It demonstrated that the array magnitude fluctuates in azimuth are within 0.25 dB, and such a variation is considered small and negligible. When the rotation step is smaller, the fluctuates will be smaller, and the absolute gain will go higher. The gain will be deducted from the final PDP. To have a fair comparison of the propagation characteristics for the twelve links and see the coverage range of the Rx antenna, the Rx antenna is placed on a tripod with a fixed location and pointing angle along $X$-axis during the whole channel measurement. The heights of Tx and Rx antennas are both 1.6 m. The Tx antenna is located at Tx1 and Tx3 which correspond to LOS and NLOS scenarios, respectively. During the measurement, the environment is kept static. The measured frequency range is from 59 to 61 GHz using 401 frequency points. The delay resolution is inverse to the measurement bandwidth. In our measurement, the delay resolution is 0.5 ns, which means that two paths with delay difference below 0.5 ns are not

resolvable. This is the delay resolution for Fourier transform. The output power of the signal generator is 13 dBm and the intermediate frequency (IF) filter bandwidth is 1 kHz. Therefore, the obtained data set from the measurement is a $25 \times 72 \times 401$ matrix. The key settings for this measurement are shown in Table I.

*2) UVA Method:* The system setup for the UVA-based channel measurement is similar to the RDA method. The Tx antenna is replaced by a hollow cube UVA formed of a monopole omnidirectional antenna. The configuration of the UVA is illustrated in Fig. 5. This method can be found in [22] and [23], but the virtual antenna array size was limited to $4 \times 4 \times 4$ in [22] and $7 \times 7$ in [23]. Because of the symmetry of the steering vector, the horizontal virtual rectangular array cannot distinguish impinging waves from above and below, and the vertical virtual rectangular array cannot distinguish impinging waves from front and back. Therefore, the UVA adopted in the measurement is formed of six surfaces of a $15 \times 15 \times 15$ cube. Each surface is either a horizontal or vertical virtual rectangular array consisting of $15 \times 15$ antenna elements. With this large 3-D virtual antenna array, the precise and high-resolution angle parameters can be estimated using high-resolution parameter estimation algorithms. The spacing between adjacent positions in each surface is 2.5 mm, i.e., a half wavelength at 60 GHz. More comprehensive channel measurement campaigns have been conducted for this method. The Rx antenna is the same 25-dBi horn antenna. The heights of Tx and Rx antennas are both 1.6 m. Twelve Tx locations are selected inside the room as shown in Fig. 1(b), which are positions of the user equipment and boresight LOS links with different Tx–Rx distances. The measured frequency range is

TABLE II
MEASUREMENT SETTINGS FOR THE UVA-BASED MEASUREMENT

| Center frequency 60 GHz | Bandwidth 2 GHz | Sampling points 401 | Output power +13 dBm |
|---|---|---|---|
| IF bandwidth 1 kHz | Tx locations and shift points in cube array Tx1-Tx12, $15 \times 15 \times 6$ | Rx antenna gain and beamwidth 25 dBi, 10° | Position spacing 2.5 mm |

from 59 to 61 GHz and 401 frequency samples have been collected. The obtained data set from the measurement is a $15 \times 15 \times 6 \times 401$ matrix for each Tx position. During the measurement, the environment is kept static. The key settings for this UVA-based measurement are shown in Table II.

### D. Measurement Methods' Comparison

The RDA-based method heavily relies on the accuracy of the measured radiation pattern of the directional antenna, while the rotation step is determined by the beamwidth of the radiation pattern. It may require long measurement time if very directional antenna is used. The highly directional antenna may not be rotated with its feeding port fixed exactly during the whole measurement. Thus, the antenna radiation pattern observed when the antenna points toward a certain direction may be different from the original radiation pattern with axis shifted. Furthermore, the cable connected to the antenna may introduce additional nonuniform phase drifts when the antenna is rotated, which is hard to calibrate [31]. But this method can provide large dynamic range of the received signal power because of high gain of the directional antenna, which is likely to be used for practical mmWave wireless communication systems with beamforming.

For the UVA-based method, due to the use of the monopole antenna, the accuracy of the radiation pattern is not so crucial and the implementation of this method is relatively easy. Though this method provides smaller dynamic range in comparison with the RDA-based method for a single PDP measurement, the averaging over the antenna array can provide an antenna array gain. The advantage of this method is that through high-resolution parameter estimation algorithms, the estimated MPC parameters can achieve high precision and resolution in angle domains, for example, 1° in azimuth and elevation angles, by using a large 3-D virtual antenna array.

### E. SAGE Algorithm

The SAGE algorithm has been studied extensively to jointly estimate high-resolution parameters of MPCs including the relative delay, AoA, AoD, Doppler frequency, and complex amplitude of impinging waves in mobile radio environments [32]. In a multiple-input single-output (MISO) scenario, the Tx is equipped with an antenna array consisting of $M$ elements located at $r_1, \ldots, r_M \in \mathrm{IR}^2$ with respect to an arbitrary reference point. The underlying channel gain is assumed to consist of a finite number $L$ of specular plane waves impinging at the Rx location. The received signal vector is [32]

$$Y(t) = \sum_{l=1}^{L} s(t; \theta_l) + \sqrt{\frac{N_0}{2}} N(t) \qquad (1)$$

where $N(t)$ is a standard $M$-D vector-valued complex white Gaussian noise with spectral height of $N_0$. Here, $s(t; \theta_l)$ is the signal contributed by the $l$th path at the output of the Rx array, i.e., an MPC, and can be expressed in vector notation [32]

$$s(t; \theta_l) \triangleq [s_1(t; \theta_l), \ldots, s_M(t; \theta_l)]^T$$
$$= c(\Omega_l)\alpha_l \exp\{j2\pi v_l t\} u(t - \tau_l) \qquad (2)$$

where $\theta_l \triangleq [\tau_l, \Omega_l, v_l, \alpha_l]$ is the vector containing the parameters of the $l$th MPC, i.e., relative delay $\tau_l$, AoD $\Omega_l$, Doppler frequency $v_l$, and complex amplitude $\alpha_l$. Because the measured channel is static, Doppler frequency is not considered in the proposed SAGE algorithm. In (2), $u(t - \tau_l)$ is the delayed version of Tx signal. The $M$-D vector-valued function $c(\Omega) \triangleq [c_1(\Omega), \ldots, c_M(\Omega)]^T$ is the steering vector of the array and its components are given by [32]

$$c_m(\Omega) \triangleq f_m(\Omega)\exp\{j2\pi v_l t \lambda^{-1}\langle e(\Omega), r_m\rangle\}, \quad \mathrm{m} = 1, \ldots, \mathrm{M}$$
$$(3)$$

with $\lambda$, $e(\Omega)$ and $f_m(\Omega)$ denoting the wavelength, the unit vector in $\mathrm{IR}^2$ pointing toward the direction determined by $\Omega$, and the complex electric field pattern of the $m$th antenna element, respectively. The SAGE algorithm is a variant of the expectation-maximization algorithm which consists of two steps: E-step and M-step. More details and implementation of the SAGE algorithm can be found in [32] and [33]. The focus of this section is the generation of steering vector of the array for different measurement methods.

For the UVA-based method

$$\langle e(\Omega), r_m\rangle = [x_m - d_x, y_m - d_y, z_m - d_z]e(\Omega) \qquad (4)$$

where

$$e(\Omega) = [\cos(\phi)\sin(\theta), \sin(\phi)\sin(\theta), \cos(\theta)]^T. \qquad (5)$$

The direction $\Omega$ is defined as a unit vector with initial point anchored at the origin of coordinate system and it is uniquely determined by its spherical coordinates $(\phi, \theta) \in [-180°, 180°) \times [0°, 180°]$ as shown in Fig. 5. The angles $\phi$ and $\theta$ are referred as the azimuth and the coelevation of $\Omega$, respectively, while $x_m$, $y_m$, and $z_m$ are the position coordinates of the $m$th antenna element. The spacing between adjacent position in each axis is half wavelength at 60 GHz, i.e., $d_x = d_y = d_z = 2.5$ mm.

For the RDA-based method, because the antenna is rotated coaxially, the spacing between different positions is assumed to be zero. Therefore, the steering vector for this method is equal to the complex electric field pattern of the $m$th antenna element, i.e., $c_m(\Omega) = f_m(\Omega)$.

In the literature, the RDA-based measurement data is often processed with simple peak search algorithm and the rotated angle is assumed to be the path AoA or AoD. This is heavily affected by the antenna characteristics. High-resolution algorithms like SAGE may be affected by phase inaccuracy, and the acquire of 3-D antenna radiation pattern in 60-GHz frequency band is also hard and time consuming. Due to the lack of accurate antenna radiation pattern, the RDA measurement data are not processed with SAGE algorithm in this paper.
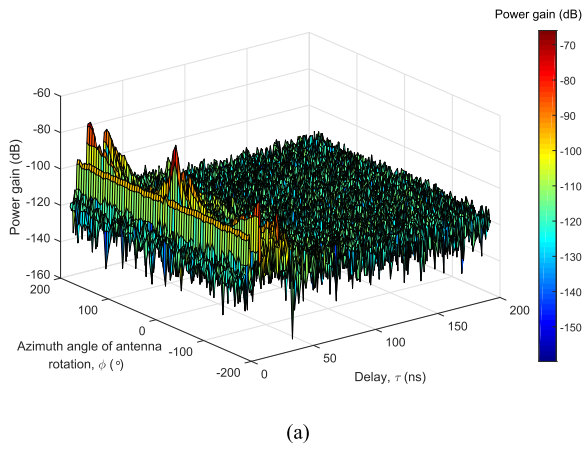
(a)
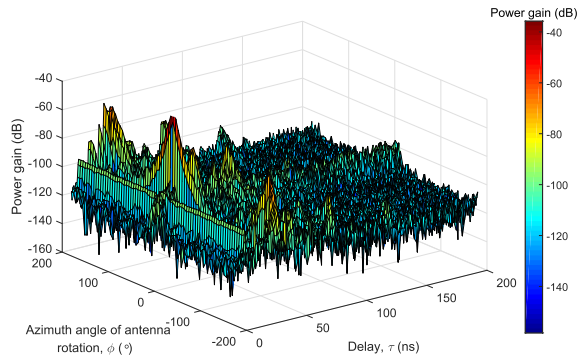


(b)

Fig. 6. Measured delay-AS function at Tx1. (a) Elevation angle = 30°. (b) Elevation angle = 90°.
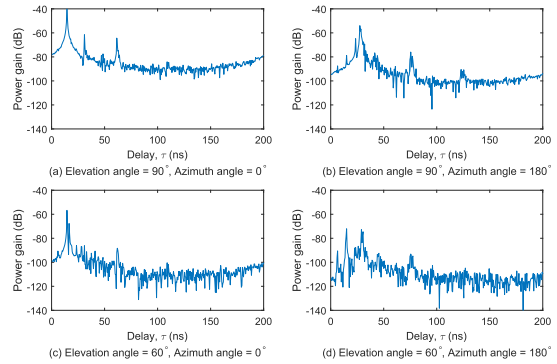


Fig. 7. Different directional PDPs at Tx1. (a) Elevation angle = 90°, azimuth angle = 0°. (b) Elevation angle = 90°, azimuth angle = 180°. (c) Elevation angle = 60° and azimuth angle = 0°. (d) Elevation angle = 60°, azimuth angle = 180°.
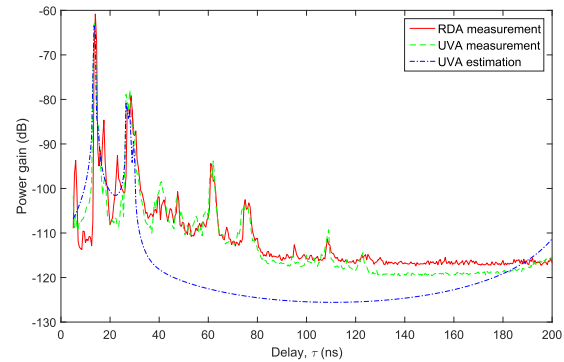


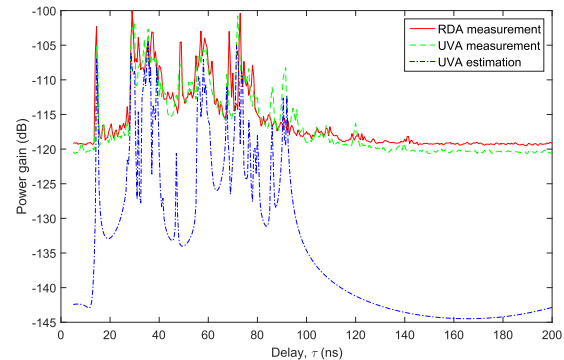Fig. 8. Average PDP for RDA- and UVA-based measurements at Tx1.



Fig. 9. Average PDP for RDA- and UVA-based measurements at Tx3.

## III. CHANNEL MEASUREMENT RESULTS

### A. RDA-Based Measurement Results

From the measurement, 1800 instantaneous directional PDPs are obtained which correspond to different Tx antenna pointing angles in azimuth and elevation. The measured delay-azimuth spread (AS) function results for 25-dBi Tx antenna at Tx1 with different elevation angles for the 60-GHz indoor channel using rotated horn antenna are shown in Fig. 6. The LOS component and MPCs are clearly identified from the measured delay-AS function. Some of the PDPs are shown in Fig. 7. The dynamic range of the measurement system is about 60 dB. A LOS component can be clearly observed when two antennas are pointing to each other with the relative received power of up to −40 dB. When antennas are misaligned, the power is reduced gradually.

To the best of our knowledge, the comparison of the RDA measurement results and UVA estimation results has never been done in the literature. To do the comparison, the RDA measurement results are compared with the UVA measurement results at Tx1 and Tx3. For LOS scenario at Tx1, the average PDPs obtained by the RDA measurement, UVA measurement, and UVA estimation are shown in Fig. 8. For the RDA measurement, the 25-dBi Tx antenna gain has been subtracted. The two average PDPs show good agreement with each other. The LOS component arrives with relative received power about −60 dB and delay of 13.5 ns, which corresponds to 4-m

separation. Another first-order reflection component at 26.5 ns in delay can also be seen with the power degradation of 20 dB compared with the LOS component. The second-order reflection at about 60 ns in delay has the power degradation of 34 dB with respect to the LOS component. Due to its weakness, this path is not estimated by the SAGE algorithm of 30-dB threshold. Later we will show that this is also due to the fact that the strong path has interference on the estimation of weak path in LOS scenario, while in NLOS scenario, all paths can be accurately estimated even with relatively weak powers, as shown in Fig. 9 for Tx3. The power azimuth profile (PAP) comparison at Tx1 is shown in Fig. 10. The PAP is obtained by summing linear power over all elevation angles for each azimuth angle using the RDA measured data,
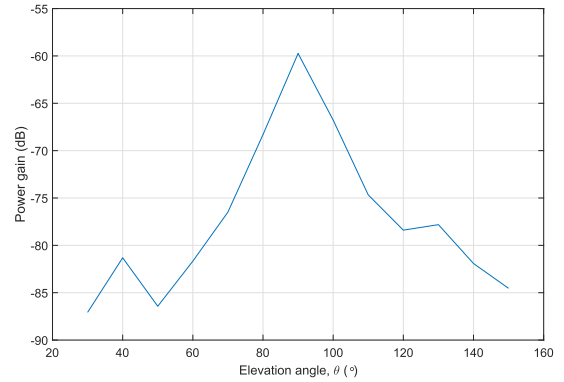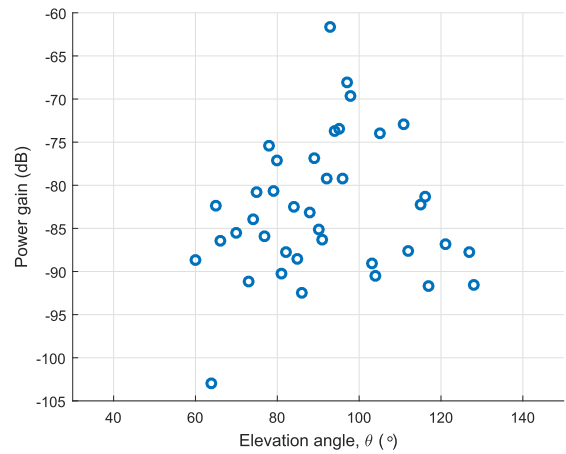
Fig. 10.   PAP comparison at Tx1. (a) RDA measurement. (b) UVA estimation.
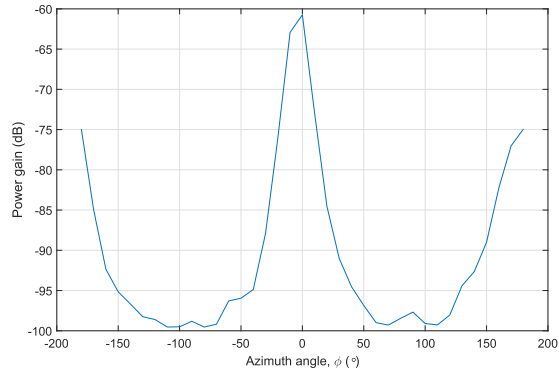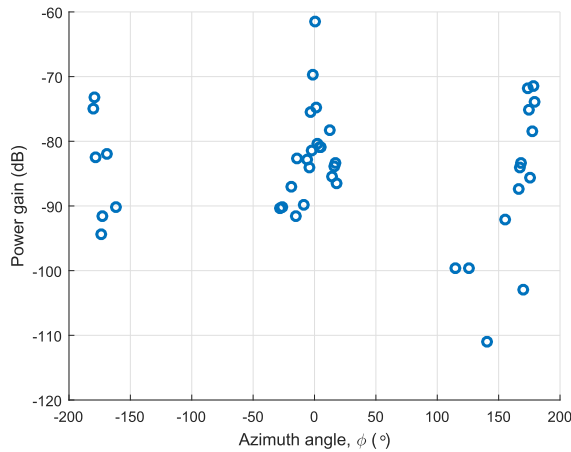


Fig. 11.   PEP comparison at Tx1. (a) RDA measurement. (b) UVA estimation.

while it is obtained by combining the SAGE estimated MPCs with the same azimuth angle but differ in delays and elevation angles. Although objects placed near the Tx may have higher order reflections and diffractions, the relative received power is relatively weak and these MPCs are not dug out by the SAGE algorithm. The power elevation profile (PEP) comparison at Tx1 is shown in Fig. 11. The PEP is obtained by summing linear power over all azimuth angles for each elevation angle, while it is obtained by combining the SAGE estimated MPCs with the same elevation angle but differ in delays and azimuth angles. We can see that the PAP and PEP obtained by the two methods match well. The LOS component departures with 0° in azimuth angle and 90° in elevation angle. The first-order reflection component departures with ±180° in azimuth angle while confined in a narrow direction range near 90° in elevation angle. However, some little differences can be seen. The UVA estimation results show relatively small elevation angle range about 60°–130° compared with the RDA measurement which shows angle range about 40°–140° with relatively strong power. The normalized PAS comparison at Tx1 is shown in Fig. 12. The PAS is obtained from the measured 1800 instantaneous directional PDPs by summing over delay domain for RDA measured data and the SAGE estimates from the UVA measured data, respectively. For RDA method, the MPC AoDs are using the antenna pointing angles on the positioner from −180° to 180° in azimuth and from

30° to 150° in elevation with a step of 5°. Except the LOS component at (azimuth angle = 0°, elevation angle = 90°), a major scatterer MPC can be observed at (azimuth angle = ±180°, elevation angle = 90°). Overall, the results obtained by the two methods show good agreement with each other in terms of the average PDP, PAP, PEP, and PAS, which verifies the validation of the two measurement methods.

### B. UVA-Based Measurement Results

In SAGE algorithm, the number of MPCs is usually predefined which is large enough to capture all the significant paths. In the literature, this large number ranges from 50 to 400. In this paper, we have changed the estimated number of paths and find out that 100 paths are appropriate to capture most of the signal energy while within an acceptable computation complexity.

Twelve Tx locations are selected in this set of measurements including LOS scenarios and NLOS scenarios. The power, AoD in azimuth and elevation, and delay of MPCs are all estimated. The K-means algorithm [34] is adopted for clustering based on delay, AoD in azimuth and elevation domains of MPCs estimated from the SAGE algorithm. A KPowerMeans algorithm was introduced in [35] based on the K-means algorithm, and considered power weight to calculate the cluster centroid and used MPC distance as a metric to combine
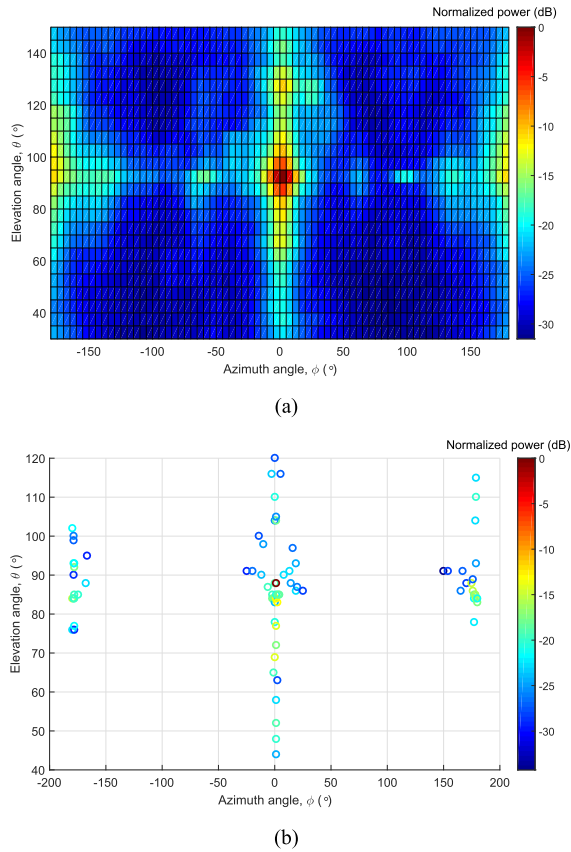
(a)



(b)

Fig. 12. PAS comparison at Tx1. (a) RDA measurement. (b) UVA estimation.
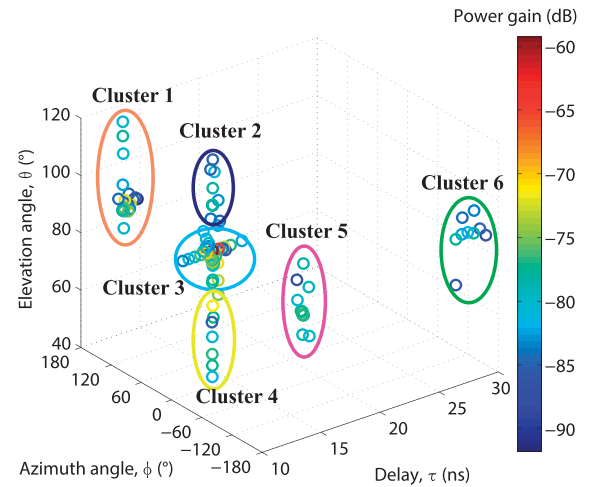


Fig. 13. MPCs and clustering results for UVA-based measurement at Tx1.



Fig. 14. Measurement setup for UVA-based measurement at Tx1.

normalized delays and angles with different units. However, the delay scale parameter is unknown and related to the real measurement data set and can highly affect the clustering results. In addition, in the extended S-V model, the powers of clusters and rays in each cluster have a decay rate, implying that powers may change greatly within a cluster. Thus, we use the traditional K-means algorithm to do the clustering instead.

There are some scientific criteria for determining the number of clusters, among which the Kims–Park (KP) index, Calinski–Harabasz index, Xie–Beni index, and PBM index are most popularly used [36], [37]. Though there are so many scientific criteria, several studies on performance comparison showed that there is no single index which outperforms all the others [37]. Besides, the optimal number may be different according to the data type in LOS and NLOS scenarios. Improvements may be achieved by combining several indices, but the weight of each index is an open question. In this paper, we chose the KP index to determine the optimal cluster number. A cluster is defined as a group of MPCs showing similar delay and AoD. Clusters should not overlap. For each identified cluster $i$, a set of parameters $C_i = (T_i, \Phi_i, \Theta_i)$ is used to approximate the center of the cluster, where $T_i$, $\Phi_i$, and $\Theta_i$ are delay, AoD in azimuth domain, and AoD in elevation domain, respectively. The center of a cluster is defined as the mean value over each domain. As shown in Fig. 13 for Tx1 position with Tx–Rx separation of 4 m, six clusters are observed, centered at approximately $C_1 = (14 \text{ ns}, 178°, 85°)$, $C_2 = (13.5 \text{ ns}, 0°, 109°)$, $C_3 = (13.5 \text{ ns}, 1°, 87°)$, $C_4 = (13.5 \text{ ns}, 1°, 57°)$, $C_5 = (13.5 \text{ ns}, -178°, 84°)$, and

$C_6 = (26.5 \text{ ns}, -178°, 91°)$. Cluster 3 is the LOS component, although it has wide angle spread in azimuth domain. From clusters 1, 2, 4, and 5 shown in Fig. 13, it can be observed that some MPCs have very different AoDs (sometimes larger than 100°) but quite close delays (less than 1 ns). Note that the antenna positioner has effects on the measured channel. This effect is hard to remove and may be modeled as stochastic scatterers. For example, the same situation can be observed in cluster 1, where the signal is reflected by the antenna support on the positioner as shown in Fig. 14. Cluster 6 is at approximately 26.5 ns which is the first-order reflection from the wall based on wave traveling distance and AoD information. Further investigation of the estimated MPCs shows that for the three boresight LOS scenarios, i.e., Tx1, Tx5, and Tx6, each position shows the two strong clusters departure with azimuth angle near 0° and ±180°, but with different delays according to different Tx antenna positions.

Fig. 15 shows the estimated MPCs and their clustering for Tx11. Six clusters are identified and their centers are approximately at $C_1 = (33 \text{ ns}, -39°, 91°)$, $C_2 = (31 \text{ ns}, -164°, 90°)$, $C_3 = (58 \text{ ns}, 79°, 98°)$, $C_4 = (58 \text{ ns}, -8°, 87°)$, $C_5 = (58 \text{ ns}, -170°, 98°)$, and $C_6 = (78.5 \text{ ns}, -174°, 91°)$. The distance between the Tx and Rx is 4 m. According to delays of MPCs, there is no LOS component. This is because of the narrow beamwidth of horn antenna at the Rx. Fig. 16 shows the synthesized PDP from the SAGE results, which collects the total power of all rays in one delay bin. It can be
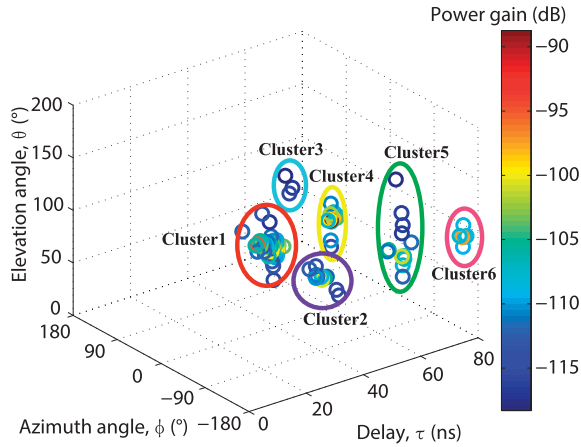
Fig. 15.   MPCs and clustering results for UVA-based measurement at Tx11.
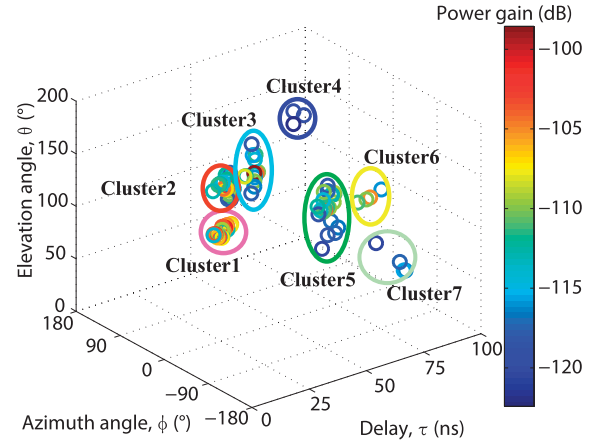


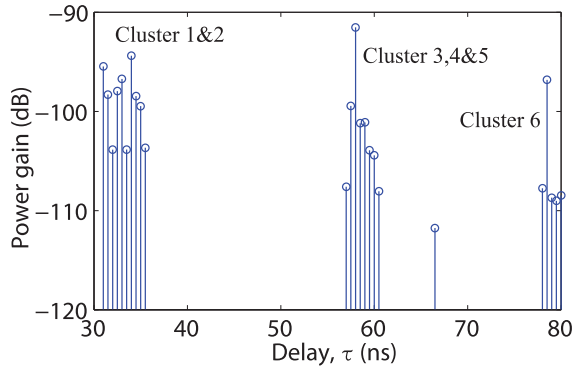Fig. 17.   MPCs and clustering results for UVA-based measurement at Tx3.



Fig. 16.   Synthesized PDP for UVA-based measurement at Tx11.

observed that clusters 1 and 2 have very close delays, so as clusters 3–5. This is probably caused by scattering from the antenna positioner. For cluster 6, its delay is about 78.5 ns, which indicates multiple reflections or scattering. In terms of power, the maximum received single ray power is −88.7 dB in cluster 4. Even having multiple reflection/scattering, the peak single ray power in cluster 6 is up to −97 dB.

Fig. 17 shows the estimated MPCs and their clustering for Tx3, which is an NLOS scenario. Seven clusters are identified. Their centers are approximately at $C_1 = (33.5$ ns, $42°$, $89°)$, $C_2 = (58$ ns, $158°$, $87°)$, $C_3 = (72$ ns, $170°$, $88°)$, $C_4 = (72$ ns, $57°$, $169°)$, $C_5 = (72.5$ ns, $11°$, $89°)$, $C_6 = (91.5$ ns, $8°$, $88°)$, and $C_7 = (72$ ns, $−174°$, $74°)$. The Tx–Rx distance in this scenario is about 4.2 m. Because the Tx and Rx antennas are at the same height, most of elevation angles of MPCs are around 90°.

The SAGE estimated MPC parameters for all the 12 Tx positions show that azimuth AoD is diverse over −180°–180° and largely related to Tx antenna position and the measurement environment, while elevation AoD is more related to the different heights of Tx and Rx antennas and confined in a relatively small direction range over 40°–120°.

## IV. 60-GHz Indoor Channel Modeling

Due to the limited measurement data in RDA measurements, the 60-GHz indoor channel modeling is mainly based on

the measured data using the UVA method. Due to large bandwidths and therefore high delay resolution in mmWave 5G communication systems, delay and angular domain cluster characteristics have been observed in our measurement results, as well as in some other measurements in the literature. The original S-V model assumes that rays arrive in clusters in the delay domain, which can easily be extended to the angular domain. In this paper, we have therefore used the extended S-V model with both delay and angular cluster characteristics.

The channel impulse response for the channel model in MISO scenario without polarization characteristics is given by [25]

$$h(t, \phi_{tx}, \theta_{tx}) = \sum_i A^{(i)} C^{(i)}\big(t - T^{(i)}, \phi_{tx} - \Phi_{tx}^{(i)}, \theta_{tx} - \Theta_{tx}^{(i)}\big)$$

(6)

with

$$C^{(i)}(t, \phi_{tx}, \theta_{tx}) = \sum_k \alpha^{(i,k)} \delta(t - \tau^{(i,k)})$$
$$\cdot \delta\big(\phi_{tx} - \phi_{tx}^{(i,k)}\big) \delta\big(\theta_{tx} - \theta_{tx}^{(i,k)}\big)$$ (7)

where $\phi_{tx}$ and $\theta_{tx}$ are azimuth and elevation angles at the Tx, respectively, $A^{(i)}$ and $C^{(i)}$ are the channel coefficient and channel gain for the $i$th cluster, respectively, $\delta()$ is the Dirac delta function, $T^{(i)}$, $\Phi_{tx}^{(i)}$, and $\Theta_{tx}^{(i)}$ are time-angular coordinates of the $i$th cluster, $\alpha^{(i,k)}$ is the amplitude of the $k$th ray of the $i$th cluster, and $\tau^{(i,k)}$, $\phi_{tx}^{(i,k)}$, and $\theta_{tx}^{(i,k)}$ are relative time-angular coordinates of the $k$th ray within the $i$th cluster.

Due to the high resolution in time and space at mmWave frequencies, the proposed channel model uses the clustering approach with each cluster consisting of several rays closely spaced in time and angular domains.

The stochastic properties of root-mean-square (RMS) delay spread (DS), AS, elevation spread (ES), as well as the inter-cluster and intracluster parameters will be calculated.

### A. RMS DS

The RMS DS is calculated based on the estimated MPCs using the SAGE algorithm, only including values having MPC

power within a certain range from the peak value. Here, a 30-dB dynamic range is applied when computing the RMS DS. The RMS DS is then calculated as [38]

$$\tau_{rms} = \sqrt{\frac{\sum_i \sum_k |\alpha^{(i,k)}|^2 (\tau^{(i,k)})^2}{\sum_i \sum_k |\alpha^{(i,k)}|^2} - \left(\frac{\sum_i \sum_k |\alpha^{(i,k)}|^2 \tau^{(i,k)}}{\sum_i \sum_k |\alpha^{(i,k)}|^2}\right)^2}. \tag{8}$$

### B. RMS AS

Both global AS (GAS) and cluster AS (CAS) are calculated using the SAGE estimates. The GAS is defined as the second-order moment of the azimuth power spectrum at the Tx side and is given by [38]

$$\phi_{rms} = \sqrt{\frac{\sum_i \sum_k |\alpha^{(i,k)}|^2 (\phi_{tx}^{(i,k)})^2}{\sum_i \sum_k |\alpha^{(i,k)}|^2} - \left(\frac{\sum_i \sum_k |\alpha^{(i,k)}|^2 \phi_{tx}^{(i,k)}}{\sum_i \sum_k |\alpha^{(i,k)}|^2}\right)^2}. \tag{9}$$

For the CAS, only those MPCs that contribute to the considered cluster are accounted. The CAS for $i$th cluster is given by [39]

$$\Phi_{rms}^{(i)} = \sqrt{\frac{\sum_k |\alpha^{(i,k)}|^2 (\phi_{tx}^{(i,k)})^2}{\sum_k |\alpha^{(i,k)}|^2} - \left(\frac{\sum_k |\alpha^{(i,k)}|^2 \phi_{tx}^{(i,k)}}{\sum_k |\alpha^{(i,k)}|^2}\right)^2}. \tag{10}$$

### C. RMS ES

The global ES (GES) and cluster ES (CES) can be calculated using equations similar to (9) and (10), respectively.

Table III summarizes the Tx positions, scenarios, Tx–Rx distances, number of clusters, DS, GAS, GES, average CAS, and average CES introduced in the previous sections. In 12 Tx positions, there are six LOS scenarios and six NLOS scenarios. Here LOS refers to the scenario where there is an unobstructed path between the Tx and Rx antennas, whereas NLOS refers to the scenario where there are obstructions between Tx and Rx. This definition is in accordance with [40]. We can see from Table III that Tx1, Tx5, and Tx6 are LOS scenarios with boresight alignment, Tx2, Tx9, and Tx10 are within the Rx directional antenna's coverage, while at other Tx antenna positions, the LOS link is too weak and out of the Rx antenna's coverage. Tx–Rx distance ranges from 2 to 6 m. Most of the estimated 100 MPCs are within the 30-dB power range. The number of clusters for each location is between 4 and 7, while the rays in each cluster can vary from 4 to 40. The RMS DS for LOS scenarios is smaller than that of NLOS scenarios, which agrees with the previous studies [23]. Also, AS is much larger than ES. The average GAS and GES are 74.0° and 6.8°, respectively. The average CAS and CES considering all measurement results are 32.6° and 4.6°, respectively. An interdependence between the cluster parameters can be observed. When global angular spread is large, its cluster angular spread is usually large as well. But some exceptions exist such as at Tx1.
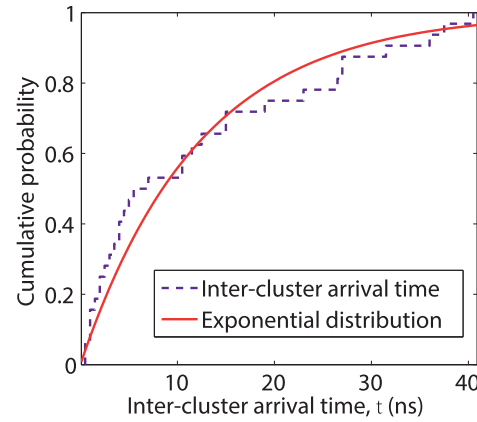


Fig. 18.  CDF of the intercluster arrival times and an exponential distribution.

### D. Intercluster Parameters

The intercluster arrival time is defined as the relative delay difference between two adjacent clusters. The delay of a cluster is taken as the delay of the strongest MPC in the cluster. Fig. 18 shows the cumulative distribution function (CDF) of the intercluster arrival rate. The distribution of the cluster arrival time is described by a Poisson process which is modeled by an exponential distribution [26]. The intercluster arrival rate $\Lambda$ can be approximated by the inverse of the mean intercluster arrival time, which is 0.08 1/ns under both LOS and NLOS scenarios. It agrees with the result of 0.07 1/ns when using omnidirectional antenna at the Tx and 15° beamwidth antenna at the Rx in an office environment [26]. The cluster power decay rate $\Gamma$ is defined as the decay rate of the strongest path within each cluster and modeled by an exponential decay. In our measurement, the power decay rate is estimated to be 2.5 ns under both LOS and NLOS scenarios.

### E. Intracluster Parameters

The intracluster parameters of the channel model are estimated from the SAGE results. The intracluster characteristics in angular domain such as CAS and CES have been studied in previous sections. This section focuses on the intracluster characteristics in time domain. Based on the identified individual rays in time domain, statistical characteristics including average number of rays, ray arrival rate, and ray power decay time are calculated. The average number of rays in each cluster is about 20. But some clusters have the number of rays less than 20. The intracluster time-domain model was proposed in [25]. The cluster consists of a central ray $\alpha^{(i,0)}$ with fixed amplitude, precursor rays $\alpha^{(i,-N_{\text{pre}})}, \ldots, \alpha^{(i,-1)}$, and postcursor rays $\alpha^{(i,1)}, \ldots, \alpha^{(i,N_{\text{post}})}$. The central ray $\alpha^{(i,0)}$ is selected as the ray with highest amplitude in the cluster. The numbers of precursor rays $N_{\text{pre}}$ and postcursor rays $N_{\text{post}}$ can be derived from measurements. Precursor and postcursor rays are modeled as two Poisson processes with arrival rates $\lambda_{\text{pre}}$ and $\lambda_{\text{post}}$, respectively. The average amplitudes $A_{\text{pre}}$ and $A_{\text{post}}$ of the precursor and postcursor rays decay exponentially with power decay times $\gamma_{\text{pre}}$ and $\gamma_{\text{post}}$, respectively. They can

TABLE III
RESULT SUMMARY: CLUSTERS, DS, AND ANGULAR SPREAD

| Position | Scenario | Distance (m) | No. of cluster | DS (ns) | GAS (°) | GES (°) | Average CAS (°) | Average CES (°) |
|---|---|---|---|---|---|---|---|---|
| Tx1 | LOS | 4.00 | 6 | 1.9 | 76.6 | 7.8 | 3.0 | 5.3 |
| Tx2 | LOS | 5.54 | 4 | 17.8 | 80.8 | 5.5 | 73.4 | 4.6 |
| Tx3 | NLOS | 4.24 | 7 | 19.8 | 66.7 | 6.4 | 35.1 | 4.5 |
| Tx4 | NLOS | 3.50 | 5 | 16.9 | 74.1 | 6.9 | 47.0 | 4.2 |
| Tx5 | LOS | 3.00 | 4 | 1.8 | 84.0 | 11.9 | 17.8 | 4.2 |
| Tx6 | LOS | 2.00 | 6 | 1.4 | 79.5 | 9.7 | 10.8 | 10.7 |
| Tx7 | NLOS | 3.08 | 5 | 9.7 | 62.5 | 7.0 | 49.1 | 4.1 |
| Tx8 | NLOS | 2.34 | 6 | 7.2 | 77.8 | 5.8 | 15.4 | 4.8 |
| Tx9 | LOS | 6.09 | 4 | 11.6 | 103.2 | 8.2 | 62.0 | 4.7 |
| Tx10 | LOS | 5.01 | 4 | 14.4 | 54.7 | 3.7 | 35.6 | 2.6 |
| Tx11 | NLOS | 4.00 | 6 | 15.2 | 55.8 | 4.4 | 26.7 | 2.0 |
| Tx12 | NLOS | 3.12 | 5 | 9.2 | 72.4 | 5.0 | 15.3 | 3.3 |
| Average | N/A | 3.83 | 5.1 | 10.6 | 74.0 | 6.8 | 32.6 | 4.6 |

TABLE IV
INTRACLUSTER TIME-DOMAIN PARAMETERS: COMPARISON WITH [23] AND IEEE802.11AD CONFERENCE ROOM MODEL

| Parameter | Notation | LOS | NLOS | LOS/obstructed LOS [23] | 802.11ad |
|---|---|---|---|---|---|
| Ray decay time | $\gamma_{pre}$ [ns] | 4 | 3.9 | 4.6/4.8 | 3.7 |
| | $\gamma_{post}$ [ns] | 5.4 | 4.5 | 4.7/4.5 | 4.5 |
| Ray K factor | $K_{pre}$ [dB] | 11.5 | 3.3 | 8.6/10.3 | 10 |
| | $K_{post}$ [dB] | 8.4 | 8.9 | 9.0/11.0 | 14.2 |
| Ray arrival rate | $\lambda_{pre}$ [1/ns] | 0.5 | 0.7 | 0.9/1.1 | 0.37 |
| | $\lambda_{post}$ [1/ns] | 0.5 | 1.2 | 0.9/1.0 | 0.31 |

be expressed as [25]

$$A_{\text{pre}}(\tau) = A_{\text{pre}}(0)e^{|\tau|/\gamma_{\text{pre}}}$$
$$A_{\text{post}}(\tau) = A_{\text{post}}(0)e^{-|\tau|/\gamma_{\text{post}}}. \tag{11}$$

Rician K-factors are defined as the ratio of the amplitude of the central ray of the cluster $\alpha^{(i,0)}$ to the amplitudes of the precursor or postcursor rays

$$K_{\text{pre}} = 20\log_{10}\left|\frac{\alpha^{(i,0)}}{A_{\text{pre}}(0)}\right| \text{(dB)}$$
$$K_{\text{post}} = 20\log_{10}\left|\frac{\alpha^{(i,0)}}{A_{\text{post}}(0)}\right| \text{(dB)}. \tag{12}$$

Table IV lists the estimated intracluster time domain parameters for the LOS and NLOS scenarios and compares them with the values from [23] and the IEEE802.11ad channel model [25] for a conference room environment. Although they are for a conference room, the size of our office room is close to theirs. Our results show larger values for the LOS postcursor ray decay time and smaller postcursor ray K factors, due to the differences in the measurement environment and the data processing method.

## V. CONCLUSION

In this paper, a signal generator-VNA-based measurement system has been established in an office environment for 60-GHz indoor channels. Measurement results generated from the RDA and UVA methods have been compared and verified. It turns out that the RDA method highly relies on the accuracy of antenna radiation pattern, while the UVA method is easier to implement and can get high precision and resolution in azimuth and elevation angular domains by using the large 3-D virtual antenna array. Measurement results with six LOS and six NLOS scenarios using the UVA method have been estimated using the SAGE algorithm, and clustered using the K-means algorithm.

The measured channel has been modeled based on an angular extended S-V model. Both intercluster and intracluster parameters have been characterized. Especially, angular characteristics including both azimuth and elevation domains in global level and cluster level have been investigated. We have found out that azimuth departure angles are diverse and highly related to antenna position and the measurement environment, while the elevation departure angles are more related to the antenna height difference and confined in a relatively small direction range. Meanwhile, the estimated AS is much larger than the ES in both global and cluster levels. Estimated parameters for cluster decay rate, cluster arrival rate, ray decay rate, Rician K-factor, and ray arrival rate have also been presented and compared with existing studies in a similar size conference room environment.

## REFERENCES

[1] C.-X. Wang, A. Ghazal, B. Ai, Y. Liu, and P. Fan, "Channel measurements and models for high-speed train communication systems: A survey," *IEEE Commun. Surveys Tuts.*, vol. 18, no. 2, pp. 974–987, 2nd Quart., 2016.
[2] C.-X. Wang, S. Wu, L. Bai, X. You, J. Wang, and C.-L. I, "Recent advances and future challenges for massive MIMO channel measurements and models," *Sci. China Inf. Sci.*, vol. 59, no. 2, pp. 1–16, Feb. 2016.
[3] L. Wei, R. Q. Hu, Y. Qian, and G. Wu, "Key elements to enable millimeter wave communications for 5G wireless systems," *IEEE Wireless Commun.*, vol. 21, no. 6, pp. 136–143, Dec. 2014.
[4] P. Smulders, "Exploiting the 60 GHz band for local wireless multimedia access: Prospects and future directions," *IEEE Commun. Mag.*, vol. 40, no. 1, pp. 140–147, Jan. 2002.
[5] *IEEE Standard for Information Technology—Telecommunications and Information Exchange Between Systems—Local and Metropolitan Area Networks—Specific Requirements. Part 15.3: Wireless Medium Access Control (MAC) and Physical Layer (PHY) Specifications for High Rate Wireless Personal Area Networks (WPANs) Amendment 2: Millimeter-wave-based Alternative Physical Layer Extension*, IEEE Standard 802.15.3c-2009 (Amendment to IEEE Standard 802.15.3-2003), Oct. 2009.

[6] IEEE Draft Standard for Local and Metropolitan Area Networks—Specific Requirements—Part 11: Wireless LAN Medium Access Control (MAC) and Physical Layer (PHY) Specifications—Amendment 3: Enhancements for Very High Throughput in the 60 GHz Band, IEEE Standard P802.11ad/D8.0, May 2012 (Draft Amendment Based on IEEE Standard 802.11-2012), Jun. 2012.

[7] T. S. Rappaport, R. W. Heath, R. C. Daniels, and J. N. Murdock, Millimeter Wave Wireless Communications. Upper Saddle River, NJ, USA: Pearson Education, 2014.

[8] W. Roh et al., "Millimeter-wave beamforming as an enabling technology for 5G cellular communications: Theoretical feasibility and prototype results," IEEE Commun. Mag., vol. 52, no. 2, pp. 106–113, Feb. 2014.

[9] T. S. Rappaport et al., "Millimeter wave mobile communications for 5G cellular: It will work!" IEEE Access, vol. 1, pp. 335–349, May 2013.

[10] T. S. Rappaport, F. Gutierrez, Jr., E. Ben-Dor, J. N. Murdock, Y. Qiao, and J. I. Tamir, "Broadband millimeter-wave propagation measurements and models using adaptive-beam antennas for outdoor urban cellular communications," IEEE Trans. Antennas Propag., vol. 61, no. 4, pp. 1850–1859, Apr. 2013.

[11] S. Rangan, T. S. Rappaport, and E. Erkip, "Millimeter-wave cellular wireless networks: Potentials and challenges," Proc. IEEE, vol. 102, no. 3, pp. 366–385, Mar. 2014.

[12] C.-X. Wang et al., "Cellular architecture and key technologies for 5G wireless communication networks," IEEE Commun. Mag., vol. 52, no. 2, pp. 122–130, Feb. 2014.

[13] P. F. M. Smulders and A. G. Wagemans, "Wideband indoor radio propagation measurements at 58 GHz," Electron. Lett., vol. 28, no. 13, pp. 1270–1272, Jun. 1992.

[14] S. Geng, J. Kivinen, X. Zhao, and P. Vainikainen, "Millimeter-wave propagation channel characterization for short-range wireless communications," IEEE Trans. Veh. Technol., vol. 58, no. 1, pp. 3–13, Jan. 2009.

[15] M. Kyro et al., "Measurement based path loss and delay spread modeling in hospital environments at 60 GHz," IEEE Trans. Wireless Commun., vol. 10, no. 8, pp. 2423–2427, Aug. 2011.

[16] S. Kato et al., "Single carrier transmission for multi-gigabit 60-GHz WPAN systems," IEEE J. Sel. Areas Commun., vol. 27, no. 8, pp. 1466–1478, Oct. 2009.

[17] C. R. Anderson and T. S. Rappaport, "In-building wideband partition loss measurements at 2.5 and 60 GHz," IEEE Trans. Wireless Commun., vol. 3, no. 3, pp. 922–928, May 2004.

[18] M. Jung, J. Kim, and Y.-K. Yoon, "Measurements of path loss in mmwave for indoor environments," in Proc. APMC, Singapore, Dec. 2009, pp. 1068–1071.

[19] S. K. Yong, P. Xia, and A. Valdes-Garcia, 60GHz Technology for Gbps WLAN and WPAN: From Theory to Practice. Hoboken, NJ, USA: Wiley, 2011.

[20] T. Manabe, Y. Miura, and T. Ihara, "Effects of antenna directivity and polarization on indoor multipath propagation characteristics at 60 GHz," IEEE J. Sel. Areas Commun., vol. 14, no. 3, pp. 441–448, Apr. 1996.

[21] H. Xu, V. Kukshya, and T. S. Rappaport, "Spatial and temporal characteristics of 60-GHz indoor channels," IEEE J. Sel. Areas Commun., vol. 20, no. 3, pp. 620–630, Apr. 2002.

[22] S. Ranvier, M. Kyro, K. Haneda, T. Mustonen, C. Icheln, and P. Vainikainen, "VNA-based wideband 60 GHz MIMO channel sounder with 3-D arrays," in Proc. RWS, San Diego, CA, USA, Jan. 2009, pp. 308–311.

[23] C. Gustafson, K. Haneda, S. Wyne, and F. Tufvesson, "On mm-wave multipath clustering and channel modeling," IEEE Trans. Antennas Propag., vol. 62, no. 3, pp. 1445–1455, Mar. 2014.

[24] A. A. M. Saleh and R. A. Valenzuela, "A statistical model for indoor multipath propagation," IEEE J. Sel. Areas Commun., vol. 5, no. 2, pp. 128–137, Feb. 1987.

[25] A. Maltsev et al., Channel Models for 60 GHz WLAN Systems, IEEE Standard 802.11-09/0334r8, May 2010.

[26] S.-K. Yong, TG3c Channel Modeling Sub-Committee Final Report, IEEE Standard 802.15-07-0584-01-003c, Mar. 2007.

[27] Y. Shoji, H. Sawada, C. S. Choi, and H. Ogawa, "A modified SV-model suitable for line-of-sight desktop usage of millimeter-wave WPAN systems," IEEE Trans. Antennas Propag., vol. 57, no. 10, pp. 2940–2948, Oct. 2009.

[28] H. Sawada, H. Nakase, S. Kato, M. Umehira, K. Sato, and H. Harada, "Impulse response model and parameters for indoor channel modeling at 60 GHz," in Proc. VTC-Spring, Taipei, Taiwan, May 2010, pp. 1–5.

[29] H. Sawada, K. Fujita, S. Kato, K. Sato, and H. Harada, "Impulse response model for the cubicle environments at 60 GHz," in Proc. APMC, Yokohama, Japan, Dec. 2010, pp. 2131–2134.

[30] D. Cassioli, "UWB moves up to mmWaves: A channel modeling perspective," in Proc. ICUWB, Bologna, Italy, Sep. 2011, pp. 521–525.

[31] X. Yin, C. Ling, and M.-D. Kim, "Experimental multipath-cluster characteristics of 28-GHz propagation channel," IEEE Access, vol. 3, pp. 3138–3150, 2015.

[32] B. H. Fleury, M. Tschudin, R. Heddergott, D. Dahlhaus, and K. I. Pedersen, "Channel parameter estimation in mobile radio environments using the SAGE algorithm," IEEE J. Sel. Areas Commun., vol. 17, no. 3, pp. 434–450, Mar. 1999.

[33] B. H. Fleury, P. Jourdan, and A. Stucki, "High-resolution channel parameter estimation for MIMO applications using the SAGE algorithm," in Proc. IZSBC, Zürich, Switzerland, Feb. 2002, pp. 301–309.

[34] J. A. Hartigan and M. A. Wong, "Algorithm AS 136: A k-means clustering algorithm," J. Roy. Statist. Soc. C (Appl. Statist.), vol. 28, no. 1, pp. 100–108, 1979.

[35] N. Czink, P. Cera, J. Salo, E. Bonek, J.-P. Nuutinen, and J. Ylitalo, "A framework for automatic clustering of parametric MIMO channel data including path powers," in Proc. IEEE 64th Veh. Technol. Conf. (VTC), Montreal, QC, Canada, Sep. 2006, pp. 1–5.

[36] S. Cheng, M.-T. Martinez-Ingles, D. P. Gaillot, J.-M. Molina-Garcia-Pardo, M. Liénard, and P. Degauque, "Performance of a novel automatic identification algorithm for the clustering of radio channel parameters," IEEE Access, vol. 3, pp. 2252–2259, Nov. 2015.

[37] S. Mota, F. Perez-Fontan, and A. Rocha, "Estimation of the number of clusters in multipath radio channel data sets," IEEE Trans. Antennas Propag., vol. 61, no. 5, pp. 2879–2883, May 2013.

[38] S. Salous, Radio Propagation Measurement and Channel Modelling. Hoboken, NJ, USA: Wiley, 2013.

[39] N. Czink, X. Yin, H. OZcelik, M. Herdin, E. Bonek, and B. H. Fleury, "Cluster characteristics in a MIMO indoor propagation environment," IEEE Trans. Wireless Commun., vol. 6, no. 4, pp. 1465–1475, Apr. 2007.

[40] S. Deng, M. K. Samimi, and T. S. Rappaport, "28 GHz and 73 GHz millimeter-wave indoor propagation measurements and path loss models," in Proc. IEEE ICCW, London, U.K., Jun. 2015, pp. 1244–1250.

**Xianyue Wu** (M'11) received the B.Eng. degree in automation and electronic electrical engineering (First Class) from the Harbin Institute of Technology, Harbin, China, and the University of Birmingham, Edgbaston, U.K., in 2009, and the Ph.D. degree from the University of Birmingham, Birmingham, U.K., in 2013, involved in antenna design and channel characterization for wireless body area networks.

From 2012 to 2013, he was a Visiting Scholar at the Charles L. Brown Department of Electrical and Computer Engineering and UVA Center for Wireless Health, University of Virginia, Charlottesville, VA, USA. From 2014 to 2015, he was a Research Associate at Heriot-Watt University, Edinburgh, U.K., involved in 5G research. Currently, he is with Huawei Technologies Co., Ltd., Shanghai Research Institute, Shanghai, China.

Dr. Wu was a recipient of the Best Student Paper Prize at the 2010 Loughborough Antennas & Propagation Conference, Honorable Mention in the Second International URSI Student Prize Paper Competition at the XXX URSI General Assembly, and the Scientific Symposium of the International Union of Radio Science and Engineering and Physical Sciences Research Council Studentship (2010–2013).

**Cheng-Xiang Wang** (S'01–M'05–SM'08–F'17) received the B.Sc. and M.Eng. degrees in communication and information systems from Shandong University, Jinan, China, in 1997 and 2000, respectively, and the Ph.D. degree in wireless communications from Aalborg University, Aalborg, Denmark, in 2004.

He has been with Heriot-Watt University, Edinburgh, U.K., since 2005, and was promoted to Professor in 2011. He is also an Honorary Fellow of the University of Edinburgh, Edinburgh, and a Chair/Guest Professor of Shandong University and Southeast University, Nanjing, China. He was a Research Fellow at the University of Agder, Grimstad, Norway, from 2001 to 2005, a Visiting Researcher at Siemens AG Mobile Phones, Munich, Germany, in 2004, and a Research Assistant at the Hamburg University of Technology, Hamburg, Germany, from 2000 to 2001. He has authored one book, one book chapter, and over 260 papers in refereed journals and conference proceedings. His current research interests include wireless channel modeling and 5G wireless communication networks, including green communications, cognitive radio networks, high mobility communication networks, massive multi-in multi-out, millimeter wave communications, and visible light communications.

Prof. Wang served or is currently serving as an Editor for 12 international journals, including the IEEE TRANSACTIONS ON VEHICULAR TECHNOLOGY (since 2011), the IEEE TRANSACTIONS ON COMMUNICATIONS (since 2015), and the IEEE TRANSACTIONS ON WIRELESS COMMUNICATIONS (2007–2009). He was the leading Guest Editor of the IEEE JOURNAL ON SELECTED AREAS IN COMMUNICATIONS, Special Issue on Vehicular Communications and Networks. He served or is serving as a TPC member, TPC Chair, and General Chair for over 80 international conferences. He received nine Best Paper Awards from the IEEE Globecom 2010, IEEE ICCT 2011, ITST 2012, IEEE VTC 2013-Spring, IWCMC 2015, IWCMC 2016, IEEE/CIC ICCC 2016, and WPMC 2016. He is a fellow of IET and HEA, and a member of the EPSRC Peer Review College.

**Jian Sun** (M'08) received the Ph.D. degree from Zhejiang University, Hangzhou, China, in 2005.

Since 2005, he has been a Lecturer with the School of Information Science and Engineering, Shandong University, Shandong, China. In 2011, he was a Visiting Scholar at Heriot-Watt University, Edinburgh, U.K., supported by the U.K.–China Science Bridges: R&D on (B)4G Wireless Mobile Communications (UC4G) project. His current research interests include the areas of signal processing for wireless communications, channel sounding and modeling, propagation measurement and parameter extraction, multi-in multi-out, and multicarrier transmission systems design and implementation.

**Jie Huang** received the bachelor's degree in information engineering from Xidian University, Xidian, China, in 2013. He is currently pursuing the Ph.D. degree in communication and information systems with Shandong University, Shandong, China.

His current research interests include millimeter wave and massive multi-in multi-out channel measurements, parameter estimation, channel modeling, and 5G wireless communications.
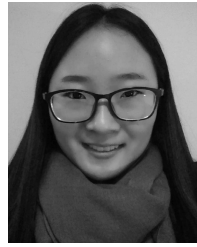
**Rui Feng** received the B.Sc. degree in communication engineering and the M.Eng. degree in signal and information processing from Yantai University, Yantai, China, in 2011 and 2014, respectively. She is currently pursuing the Ph.D. degree with the School of Information Science and Engineering, Shandong University, Shandong, China.

Her current research interests include channel parameter estimation, millimeter wave and massive multi-in multi-out channel measurements, and modeling.

**Yang Yang** ((S'99–M'02–SM'10)) received the B.Eng. and M.Eng. degrees in radio engineering from Southeast University, Nanjing, China, in 1996 and 1999, respectively, and the Ph.D. degree in information engineering from The Chinese University of Hong Kong, Hong Kong, in 2002.

He has served the Department of Electronic and Electrical Engineering, University College London, London, U.K., as a Senior Lecturer; the Department of Electronic and Computer Engineering at Brunel University, Uxbridge, U.K., as a Lecturer; and the Department of Information Engineering, The Chinese University of Hong Kong, as an Assistant Professor. He is currently a Professor with the Shanghai Institute of Microsystem and Information Technology, Chinese Academy of Sciences (CAS), Shanghai, China, serving as the Director of the CAS Key Laboratory of Wireless Sensor Network and the Communication, and the Director of the Shanghai Research Center for Wireless Communications. He is also an Adjunct Professor with the School of Information Science and Technology, ShanghaiTech University, Shanghai, China. He has co-edited a book *Heterogeneous Cellular Networks: Theory, Simulation and Deployment* (Cambridge University Press, 2013) and has co-authored more than 100 technical papers. His current research interests include wireless *ad hoc* and sensor networks, software defined wireless networks, 5G mobile systems, intelligent transport systems, wireless testbed development, and practical experiments.

Dr. Yang has been serving on the organization teams of about 50 international conferences, e.g., a Co-Chair of Ad hoc and the Sensor Networking Symposium at the IEEE ICC'15 and the Communication and Information System Security Symposium at the IEEE Globecom'15.

**Xiaohu Ge** (M'09–SM'11) received the Ph.D. degree in communication and information engineering from the Huazhong University of Science and Technology (HUST), Wuhan, China, in 2003.

He was a Researcher at Ajou University, Suwon, South Korea, and the Polytechnic University of Turin, Turin, Italy, from 2004 to 2005. Since 2005, he has been with HUST, where he is currently a Full Professor with the School of Electronic Information and Communications. He is an Adjunct Professor with the Faculty of Engineering and Information Technology, University of Technology Sydney, Ultimo, NSW, Australia. He is also the Director of the China International Joint Research Center of Green Communications and Networking. He has authored more than 130 papers in refereed journals and conference proceedings and has been granted about 15 patents in China. His current research interests include the area of mobile communications, traffic modeling in wireless networks, green communications, and interference modeling in wireless communications.

Dr. Ge is a Senior Member of the China Institute of Communications and a member of the National Natural Science Foundation of China and the Chinese Ministry of Science and Technology Peer Review College. He has been actively involved in organizing more than ten international conferences since 2005. He served as the general Chair of the 2015 IEEE International Conference on Green Computing and Communications. He serves as an Associate Editor of the IEEE TRANSACTIONS ON GREEN COMMUNICATIONS AND NETWORKING. He received the Best Paper Awards from the IEEE Globecom 2010.